CrossMark

RESEARCH ARTICLE

Volumetric imaging with homogenised excitation and static field at 9.4 T

Desmond H. Y. Tse[1] · **Christopher J. Wiggins**[2] · **Dimo Ivanov**[1] · **Daniel Brenner**[3] ·
Jens Hoffmann[4] · **Christian Mirkes**[4,5] · **Gunamony Shajan**[4] · **Klaus Scheffler**[4,5] ·
Kâmil Uludağ[1,2] · **Benedikt A. Poser**[1]

Abstract

Objectives To overcome the challenges of B_0 and RF excitation inhomogeneity at ultra-high field MRI, a workflow for volumetric B_0 and flip-angle homogenisation was implemented on a human 9.4 T scanner.

Materials and methods Imaging was performed with a 9.4 T human MR scanner (Siemens Medical Solutions, Erlangen, Germany) using a 16-channel parallel transmission system. B_0- and B_1-mapping were done using a dual-echo GRE and transmit phase-encoded DREAM, respectively. B_0 shims and a small-tip-angle-approximation kT-points pulse were calculated with an off-line routine and applied to acquire T_1- and T_2^*-weighted images with MPRAGE and 3D EPI, respectively.

Results Over six in vivo acquisitions, the B_0-distribution in a region-of-interest defined by a brain mask was reduced down to a full-width-half-maximum of 0.10 ± 0.01 ppm (39 ± 2 Hz). Utilising the kT-points pulses, the normalised RMSE of the excitation was decreased from CP-mode's 30.5 ± 0.9 to 9.2 ± 0.7 % with all B_1^+ voids eliminated. The SNR inhomogeneities and contrast variations in the T_1- and T_2^*-weighted volumetric images were greatly reduced which led to successful tissue segmentation of the T_1-weighted image.

Conclusion A 15-minute B_0- and flip-angle homogenisation workflow, including the B_0- and B_1-map acquisitions, was successfully implemented and enabled us to reduce intensity and contrast variations as well as echo-planar image distortions in 9.4 T images.

Introduction

The increased signal-to-noise ratio (SNR) [1–3] and contrast-to-noise ratio (CNR) [4] of ultra-high field (UHF) MRI provide a platform for imaging at higher resolution [5], allowing both structural [6, 7], and functional [8–10] details to be observed down to cortical layers. The increased field-induced susceptibility contrast also opens up new opportunities in T_2^*- and susceptibility weighted imaging (SWI) as well as for quantitative susceptibility mapping (QSM) [11–14]. Novel contrast mechanisms also come into play, such as the anisotropic susceptibility of white matter [15–17].

However, in order to fully take advantage of the increased SNR and CNR in UHF MRI, especially for whole brain and body imaging, one must overcome the RF inhomogeneity at UHF. At field strengths of 3 T and beyond, the RF wavelength in vivo becomes comparable to, or smaller than, the dimension of the imaging object [18–25]. This leads to interferences in the transmitted RF (B_1^+) field and results in strong intensity and contrast variations in the final image [24]. The severity of the RF inhomogeneity

✉ Desmond H. Y. Tse
desmond.tse@maastrichtuniversity.nl

1 Faculty of Psychology and Neuroscience, Maastricht University, Maastricht, The Netherlands

2 Scannexus BV, Maastricht, The Netherlands

3 German Centre for Neurodegenerative Diseases (DZNE), Bonn, Germany

4 High Field MR Center, Max Planck Institute for Biological Cybernetics, Tuebingen, Germany

5 Department for Biomedical Magnetic Resonance, University of Tuebingen, Tuebingen, Germany

increases as the RF wavelength reduces with field strength, e.g., from 7 T to 9.4 T [25].

These challenges can be addressed in several ways: RF coil [18], dielectric pads [26, 27], as well as RF pulse design [28] and parallel transmission with B_1 shimming [25, 29–31] or transmit sensitivity encoding (Transmit-SENSE) [32–34] have been proposed as possible solutions to the problem of RF inhomogeneity at UHF. Small-tip-angle (STA) pulses can, for example, be designed using the spatial domain method [32] with magnitude least square optimisation [35] in combination with k-space trajectories such as kT-points [36] or spiral nonselective (SPINS) [37]. Both kT-points and SPINS pulses have been shown to be effective in ameliorating RF inhomogeneities and have been used in Magnetisation Prepared Rapid Acquisition Gradient Echo (MPRAGE) [38] for T_1-weighted anatomical imaging [39, 40].

Benefits and challenges of UHF both include the increased effects of magnetic susceptibility and the change in relaxation times that improve various contrasts, but the downside is stronger image distortion [41], blurring and signal losses [42] due to B_0-inhomogeneity. B_0-inhomogeneities at UHF present a significant challenge especially in the context of echo planar imaging (EPI) [43] which is the sequence of choice in functional MRI and other rapid imaging applications. Furthermore, spatial variation in B_0 influences the performance of the RF excitation. B_0 variation can be alleviated with higher-order shim coils such as the 3rd and 4th orders, which have been shown to provide significant improvements in both global and local B_0 homogeneity [44].

Here, we demonstrate a B_0- and flip-angle-homogenisation workflow as implemented on a human 9.4 T scanner, to address the aforementioned challenges of UHF MRI. The B_0-shimming workflow uses a field-map-based shimming technique that homogenises the static B_0-field in a region defined by an interactively generated brain mask down to 0.12 ppm (48.0 Hz), utilising shim coils up to (partial) 3rd order. The flip-angle-homogenisation workflow takes in a B_0 map from the shimmed field and channel-by-channel complex B_1^+ maps, both measured as part of the calibration routine. Parallel RF pulses are then calculated using STA approximation, which can then be applied on the scanner with modified sequences. The workflow is presented by the example of volumetric kT-points excitation pulses. Sample T_1-weighted MPRAGE [38] and T_2^*-weighted 3D EPI [45] images collected in conjunction with the B_0- and flip-angle-homogenisation routine are shown.

Materials and methods

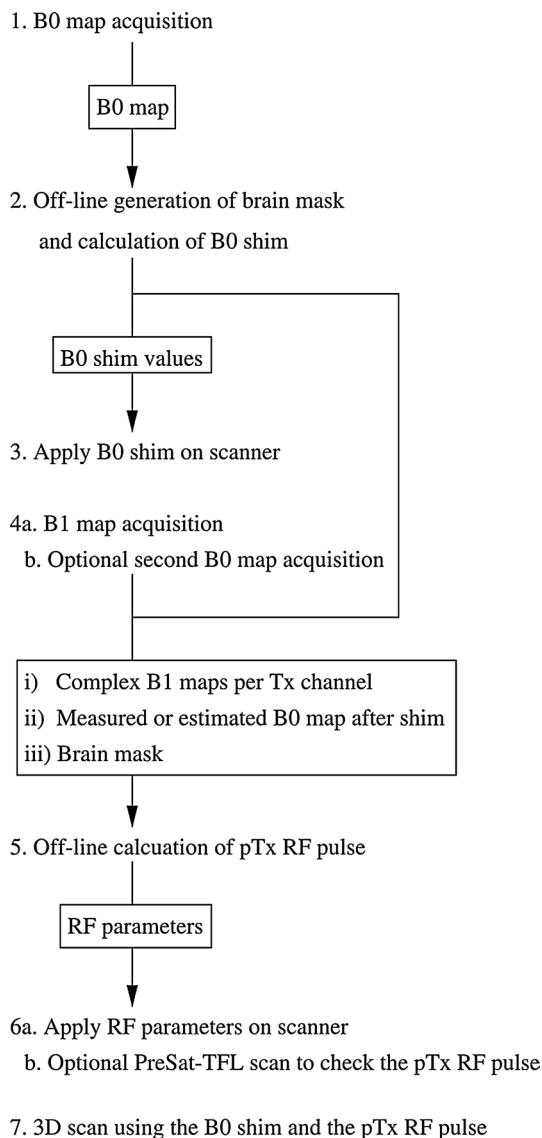All experiments were performed on a 9.4 T human MR scanner (Siemens Medical Solutions, Erlangen, Germany) using a head gradient set (AC84-mk2, maximum amplitude 80 mT/m, maximum slew rate 333 T/m/s, inner diameter 36 cm) in combination with a 16-channel parallel transmission system (1 kW per channel) and a dual-row 16-channel transmit/31-channel receive array coil [46]. Online local SAR monitoring was achieved by a vendor-provided system installed on the transmit chain [47]. The SAR matrices used for the online local SAR monitoring were derived from an EM simulation [30] on an adult male model (Hugo) with safety margins (a factor of 2) and limits set according to [48] and compressed according to the virtual observation points (VOPs) method [49]. A common model was used for all subjects. The same VOPs compressed SAR matrices were used in SAR prediction in the off-line pulse calculations and simulations. All in vivo experiments were approved by the local ethics committee and performed in accordance with internal safety guidelines and all participating volunteers gave written informed consent.

B_0- and flip-angle-homogenisation workflow

The volumetric B_0- and flip-angle-homogenisation workflow consists of calibration scans, B_0-shim and RF calculations, and optional extra B_0 and pTx RF pulse flip angle mappings for validation. The workflow is summarised in Fig. 1. All off-line calculations are carried out in MATLAB (MathWorks, Natick, MA US).

Calibration scans

B_0 field maps were obtained from a dual-echo 3D GRE sequence (TR = 30 ms, TE_1 = 1.00 ms, TE_2 = 3.21 ms, nominal flip-angle = 8 degrees, nominal voxel size = 4 mm isotropic, matrix size 50 × 50 × 44, bandwidth 1560 Hz/pixel, total scan duration 1:49 min). B_0 shimming including some 3rd order terms (Z3, Z2X, Z2Y, ZX2Y2) was accomplished with a custom software [50]. The B_0 shim routine unwraps the measured fieldmap [51] and fits spherical harmonics basis functions up to all 4th orders to it. Including the extra harmonics terms, it allows us to take some of the deviation of the physical shim coils from the spherical harmonics basis functions into account. The spherical harmonics terms for the shim coils had previously been determined by one-off calibration measurement, and were used to calculate the required shim currents to achieve field optimisation in the target region typically by a least-square fit to the in-session measured fieldmap. In order to take the system's shim current limits into account, a constrained optimisation routine provided by CVX [52, 53] was used in the shim current calculation. The target region for B_0 shimming was defined by a brain mask generated from the magnitude images of the dual-echo GRE using FSL-BET [54]. A second B_0 field map was acquired after applying the shim values in order to take the new B_0 field distribution into

1. B0 map acquisition

$\boxed{\text{B0 map}}$

2. Off-line generation of brain mask
   and calculation of B0 shim

$\boxed{\text{B0 shim values}}$

3. Apply B0 shim on scanner

4a. B1 map acquisition
   b. Optional second B0 map acquisition

$\boxed{\begin{array}{l}\text{i) Complex B1 maps per Tx channel} \\ \text{ii) Measured or estimated B0 map after shim} \\ \text{iii) Brain mask}\end{array}}$

5. Off-line calcuation of pTx RF pulse

$\boxed{\text{RF parameters}}$

6a. Apply RF parameters on scanner
   b. Optional PreSat-TFL scan to check the pTx RF pulse

7. 3D scan using the B0 shim and the pTx RF pulse

Fig. 1 The volumetric B_0 and flip-angle homogenisation workflow

account in the RF pulse calculation. This step is optional as the B_0 shim routine can also generate a predicted B_0 map after shimming for later pulse calculation.

Complex B_1 maps from all the transmit channels were obtained using a transmit phase-encoded [55], T_2 and T_2^* compensated version of DREAM [56] (imaging train repetition time = 6.8 ms, TR = 7.5 s, TE_1 = 2.22 ms, TE_2 = 4.44 ms, nominal imaging flip-angle = 7 degrees, nominal preparation pulse FA = 55.5 degrees, imaging slice thickness 4 mm, slice separation 10 mm, preparation pulse slice thickness 8 mm, voxel size 4 mm isotropic, matrix size 64 × 56 × 15, bandwidth 690 Hz/pixel, 32 transmit phase encode steps, total scan duration 4:00 min). After the pulse calculation (see below), the flip angle of the RF pulse was mapped by an implementation of the

pre-saturation turbo-flash (PreSat-TFL) sequence [57] to verify it against the prediction of the optimisation algorithm. The PreSat-TFL method parameters were: imaging train repetition time 5.9 ms, TR 10 s, TE 2.24 ms, nominal imaging FA 8 degrees, nominal preparation pulse FA 45 degrees, imaging slice thickness 4 mm, voxel size 4 mm isotropic, matrix size = 64 × 64 × 1, bandwidth 690 Hz/pixel, total scan duration 20 s.

RF pulse calculation

The parallel transmit excitation pulses utilised in the imaging sequences were designed using the spatial domain method [32] with magnitude least square optimisation [35] under the small tip-angle approximation. The optimisation was done using a conjugate-gradients-based algorithm [58] which includes a global SAR regularisation and a local SAR regularisation by means of a VOP-compressed SAR matrix [59]. Localised B_1^+ drop-out in the optimisation solution was avoided by using a region growing algorithm [60]. kT-points [36] were used as the k-space trajectory for the excitation pulses.

The kT-points trajectory consists of six equidistant points placed on the kx, ky and kz axes at ± 6.33 m^{-1}, which is roughly the inverse of the RF wavelength at 9.4 T [61], plus two additional points at the k-space centre at the beginning and the end of the trajectory. This trajectory equates to eight rectangular sub-pulses of duration 210 us interleaved with 70 us gradient blips. The RF waveform was divided into rectangular sub-pulses and played out between the gradient blips. The overall pulse duration was 2.24 ms. The trajectory, gradient blips and a RF pulse are shown in Fig. 2.

Imaging scans

MPRAGE scans were acquired using: TR = 3.75 s, TE = 3.64 ms, TI = 1.2 s, matrix size 384 × 384 × 256, voxel size 0.6 mm isotropic, sagittal slices and anterior-to-posterior phase encode direction, slice partial Fourier 7/8, echo train length = 2.1 s, nominal flip-angle = 5 degrees, GRAPPA parallel imaging using factor 3 along the in-plane phase encoding direction with 24 reference lines, bandwidth 180 Hz/pixel; total scan duration was 8:58 min. The T_1-weighting in MPRAGE was achieved by an adiabatic inversion pulse. Here, the same complex RF waveform was applied in all transmit channels, i.e., only the channel relative phases were adjusted to achieve a CP-like mode of the coil. The nominal flip-angle of the CP-mode pulse was defined as the average flip angle in a central region around the bright CP-mode spot in the middle of the brain. The inversion pulse used in the experiment was a 13 ms TR-FOCI adiabatic pulse with a peak voltage of
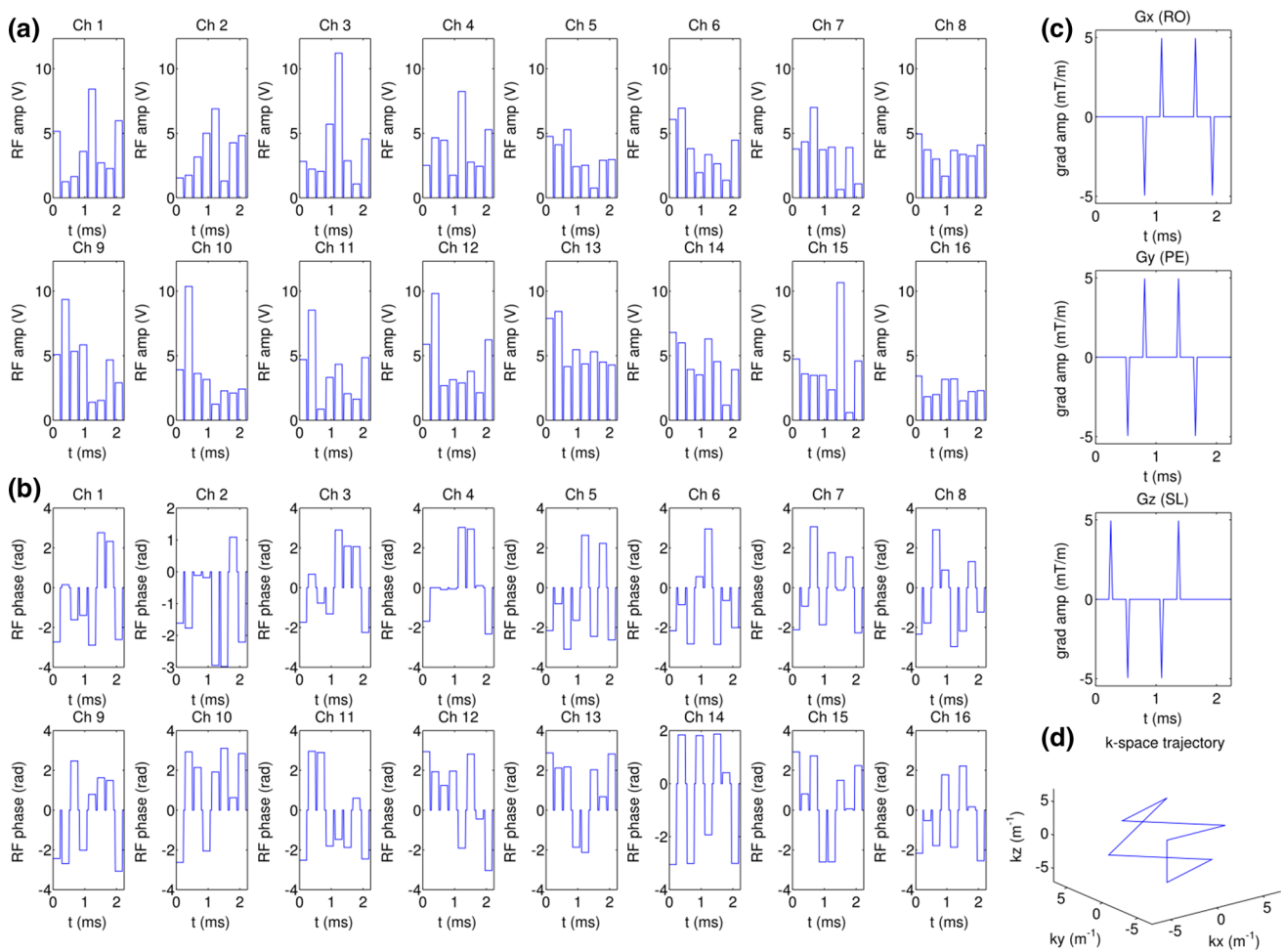
Fig. 2 a, b Channel-by-channel RF. **a** amplitudes and **b** phases from an 8-point kT-points pulse of total duration 2.24 ms. **c** The gradient blips correspond to the 8-point kT-point trajectory. **d** The k-space trajectory of the 8-point kT-points pulse which starts and ends at the k-space centre

79.8 V applied to each transmit channel (yielding a nominal peak B_1 amplitude of 10 uT) [62]. An additional proton-density-weighted image was acquired for receive bias-field correction by switching off the inversion pulse and minimising TE and TR while keeping the other parameters unchanged. For one-off comparison, the same acquisitions were repeated using a standard non-selective RF excitation pulse of 0.10 ms duration in the same CP-like mode as used for the TR-FOCI inversion pulse. For this set of MPRAGE sequence parameters, the maximum 10 g averaged local SAR per TR estimated by using the VOPs compressed SAR matrices were 0.77 and 1.11 W/kg for the kT-points and the CP-like mode excitation pulses, respectively, and was 6.77 W/kg for the TR-FOCI inversion pulse.

The T_1-weighted MPRAGE image was segmented into grey matter, white matter and cerebrospinal fluid maps with FSL-FAST [63] in a sequence of customised steps. First, the T_1-weighted image was realigned rigidly to and divided by the proton-density image to remove any intensity bias

introduced by receive field inhomogeneity [64]. Second, the co-registered proton-density image was corrected for bias fields with FSL-FAST and then passed to FSL-BET to create a brain mask. Third, the brain mask was then used to extract the brain region from the bias-corrected T_1-weighted image. Finally, the brain extracted T_1-weighted image was passed to FSL-FAST for tissue segmentation.

The same kT-points excitation was also applied in a 3D EPI sequence [45] with parameters as follows: TR = 61 ms, effective volume TR = 12.7 s, TE = 22 ms, matrix size $256 \times 256 \times 208$, voxel size 0.75 mm isotropic, phase partial Fourier 6/8, nominal flip-angle 15 degrees, bandwidth 1396 Hz/pixel, and parallel imaging undersampling with GRAPPA factor 3 along the in-plane phase-encoding direction using 96/48 reference lines/partitions that were acquired in a segmented lines-in-partition order [65]. The total acquisition time was 1:28 min. This acquisition was also repeated in a CP-like mode transmission using a 1.0 ms duration rectangular pulse. With the given 3D EPI sequence

parameters, the maximum 10 g averaged local SAR per TR were estimated to be 1.56 and 1.12 W/kg for the kT-points and the CP-like mode excitation pulses, respectively. The 3D EPI sequence was implemented such that each excitation yielded a kx-ky plane at a different kz increment, using linear ordering. Each readout was preceded by a three-lobed non-phase-encoded navigator readout at minimum TE, which served the dual purpose of EPI eddy current (Nyquist N/2 ghost) correction [66] and correction of B_0-drift due to subject breathing during the acquisition [67].

Results

Figure 3 shows the B_0 shimming results from an example set of in vivo measurement using the shim routine described above. Using only 1st and 2nd order shim coils, shimming reduces the standard deviation of the B_0 field within the brain mask to 50.1 Hz with a 90th percentile range of 148.0 Hz; when adding the four available 3rd shim coils (Z3, Z2X, Z2Y, ZX2Y2), the standard deviation and the 90th percentile range were reduced to 46.1 and 138.6 Hz, respectively.

Illustrations of the flip-angle homogenisation from the same measurement session are shown in Fig. 4. The top row shows the B_1^+ magnitude distribution of the CP-like-mode, which has a normalised RMSE of 33.3 %. The middle row of Fig. 4 is the flip-angle prediction of the MLS optimised 8-point kT-points pulse, which has a normalised RMSE of 9.1 %, and the bottom row is the pulse's corresponding single-slice flip-angle distribution measured by the PreSat-TFL in sagittal orientation. In both B_0 and flip-angle homogenisation, the measured B_0 and the flip angle distribution visually agrees very well with their predictions.
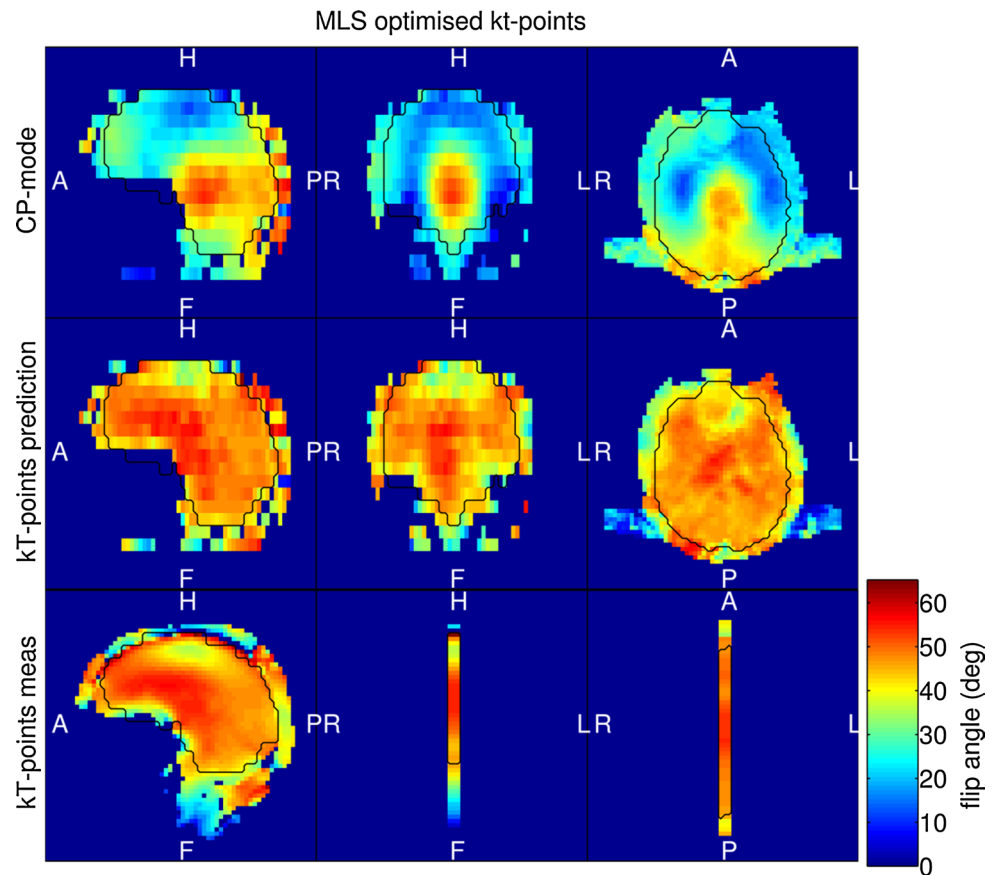
The top row of Fig. 5 shows the post hoc Bloch simulations of the TR-FOCI adiabatic pulse and the vendor's
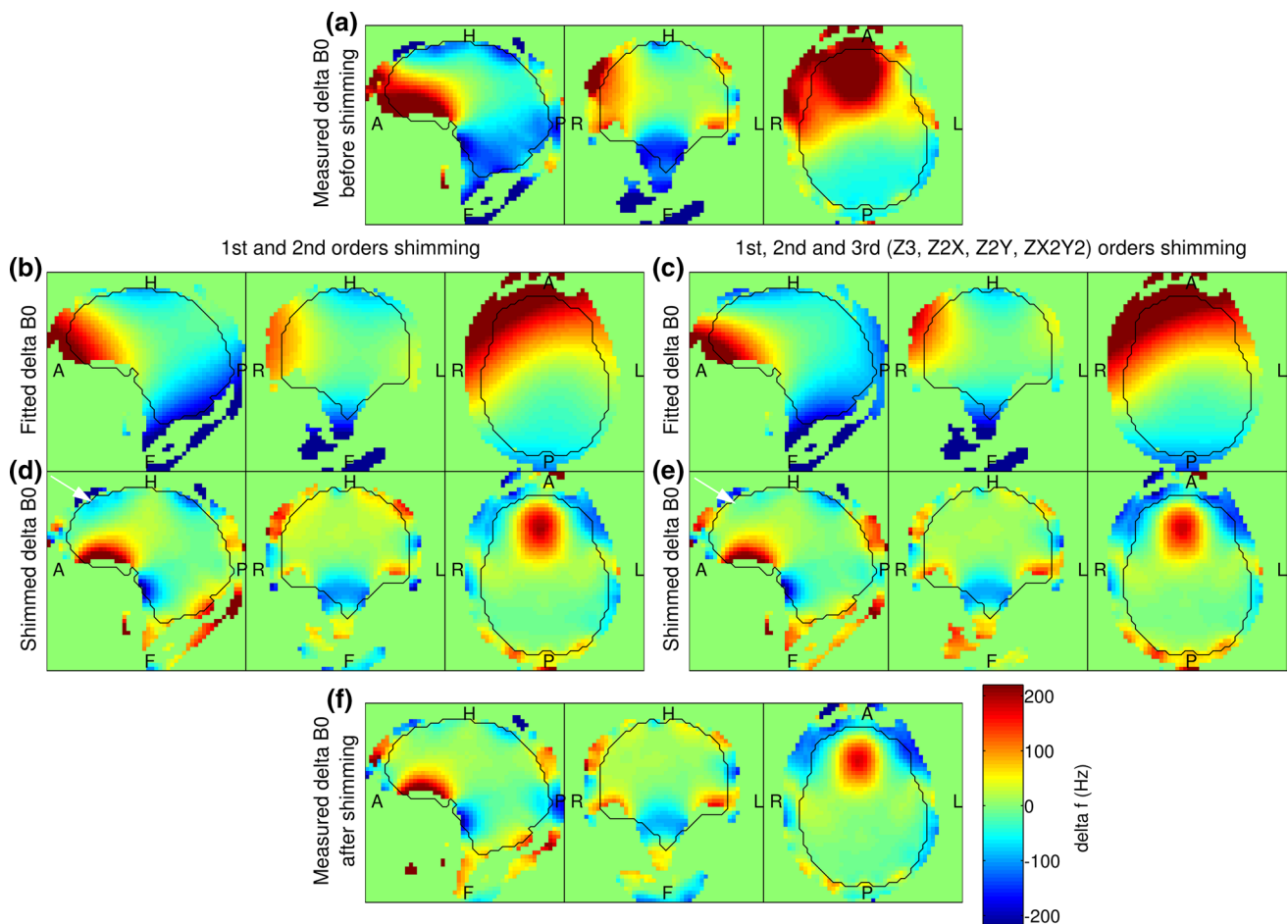

Fig. 3 **a** B_0 map derived from a 3D dual-echo GRE under the tune-up shim setting. **b** The fitted B_0 using the available fields from all the 1st and 2nd order shim coils. **c** The fitted B_0 field using all the available fields from the 1st and 2nd order shim coils, and four 3rd order shim coils: Z3, Z2X, Z2Y, ZX2Y2. **d** Prediction of the shimmed B_0 field using shim coils up to 2nd order. **e** Prediction of the shimmed B_0 field using all available shim coils up to the 3rd order. The *white arrows* in the sagittal view of **d**, **e** indicate the difference in the shim results in the frontal lobe. **f** B_0 map measured after applying the shim values from **e**

MLS optimised kt-points

Fig. 5 Achieved flip-angle as result of Bloch simulation for *top row* TR-FOCI adiabatic inversion pulse (79.8 V); *bottom row* standard hyperbolic secant adiabatic inversion pulse (166.0 V)

Bloch simulation of adiabatic inversion in CP-mode
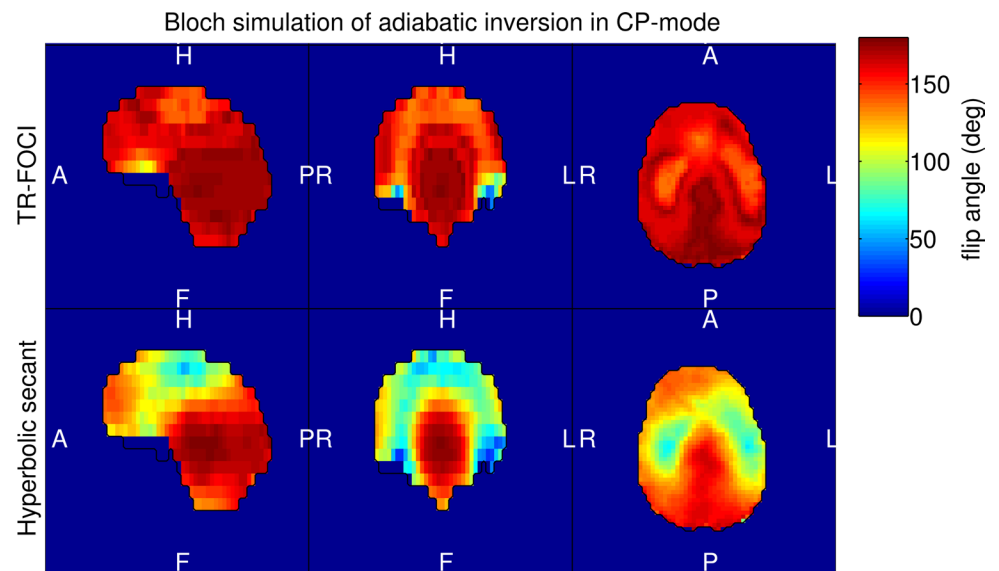
standard 5.12 ms duration hyperbolic-secant adiabatic pulse [68]. They were simulated using the subject-specific B_0 and B_1 maps collected in the same session. The pulse amplitude of the TR-FOCI and the hyperbolic secant inversion pulses were 79.8 and 166.0 V, respectively. The lower adiabatic threshold of the TR-FOCI allowed it to achieve

at least partial magnetisation inversion in regions with low field intensities in the CP-mode pattern. In contrast, large regions of brain, especially near the temporal lobes, were not inverted by the hyperbolic secant adiabatic pulse. The normalised RMSE of the TR-FOCI and hyperbolic secant inversions were 10.6 and 26.5 %, respectively. Given this

Fig. 6 *Box plots* of **a** the standard deviation and **b** the 90th percentile range of B_0 distributions after shimming with and without including the 3rd order coils; and the normalised RMSE of **c** the CP-mode and kT-points excitation pulses and **d** the Hyperbolic secant and TR-FOCI inversion pulses. In *each box*, the central mark is the median; the *edges of the box* are the 25th and 75th percentiles. The *whiskers* extend to the most extreme values which are not outliers, and the *outliers* are plotted as *red crosses* individually
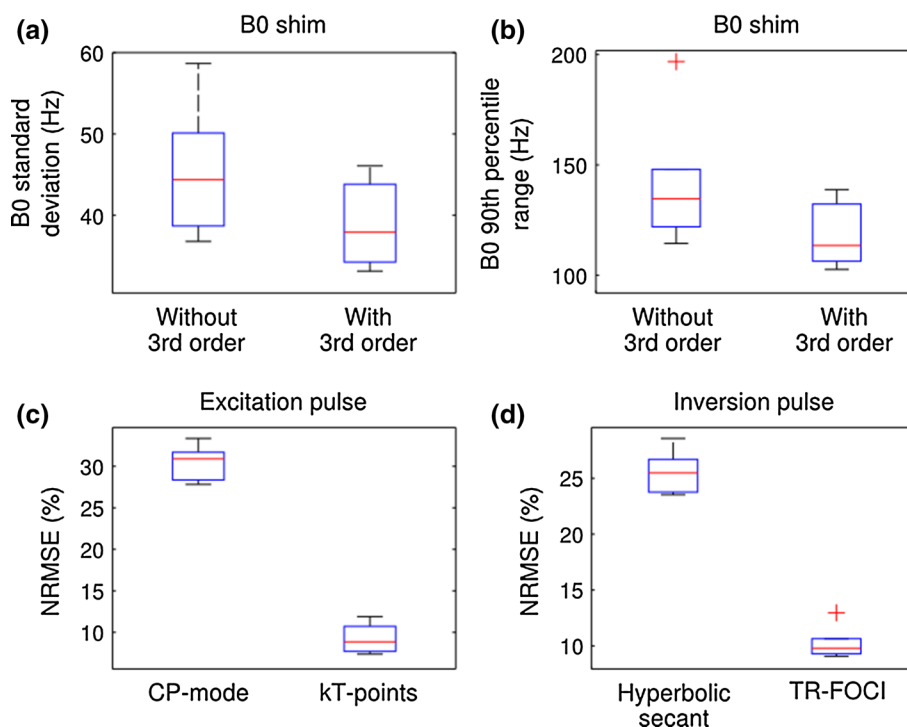
superior inversion performance of the TR-FOCI pulse it was used in all the following MPRAGE measurements.

The B_0 shim and RF pulses performances over a set of 6 in vivo measurements are summarised Fig. 6. On average, using only 1st and 2nd orders shim coils, the standard deviation and the 90th percentile range of the B_0 distribution after shim were 45.5 ± 3.2 and 141.7 ± 12.0 Hz, respectively. Including the 3rd order coils reduced them to 38.8 ± 2.1 and 117.9 ± 6.1 Hz, respectively. The average normalised RMSE of the excitation pulses were 30.5 ± 0.9 % and 9.2 ± 0.7 %, respectively, for CP-mode and kT-points; and they were 25.6 ± 0.9 and 10.3 ± 0.6 %, respectively, for hyperbolic secant and TR-FOCI inversion pulses.

Figure 7a and b show the T_1-weighted MPRAGE images using TR-FOCI inversion with CP-mode (left column) and kT-points (right column) excitation pulses for the imaging trains. The T_1-weighted and the proton density images were co-registered and divided to remove the receive bias fields. The brain-extracted and receive-bias-free images are displayed in Fig. 7c). These images were segmented by FSL-FAST into grey matter, white matter and cerebrospinal fluid maps which are shown in Fig. 7d, e and f, respectively.

B_1^+ voids, SNR and contrast variations due to B_1^+ inhomogeneity can be seen in the CP-mode T_1-weighted and proton density images. Consequently, in several regions proper segmentation of grey matter and CSF was not possible.

Results of the 3D EPI scan are shown in Fig. 8. The top and bottom rows are 3D EPI images obtained using CP-mode and kT-points excitations, respectively. Similar to the MPRAGE images, signal and contrast variations can be seen in the CP-mode image.

Discussion

B_0- and B_1-inhomogeneities are the well-known challenges in UHF MRI. Here, we presented the workflow used at our institution to homogenise both B_0 and the excitation flip-angle, allowing us to acquire high quality volumetric images at 9.4 T and further explore the potential of UHF imaging. The entire B_0 and B_1 calibration workflow currently takes approximately 15 min in total, including the (~6 min) B_0 and B_1 maps acquisitions. With further developments such as incorporating the B_0 and B_1 mapping into the scanner's on-line image reconstructions and further streamlining the data transfer between the scanner's host computer and the PC on which the B_0 and B_1 shim calculations are performed, we expect that the total calibration time can be shortened to approximately 8 min. This is only a small proportion of time typically allocated for UHF MRI studies.

The first benefit that the homogenisation workflow can bring to single- and multi-channel transmission systems alike is the potential reduction in signal loss, T_2^* blurring and distortion due to B_0 inhomogeneity, especially for the case of EPI [69]. By using a 'brain-only' region of interest and precisely calibrated shim coils, the B_0 linewidth in the brain was brought down to 39 ± 2 Hz (0.10 ± 0.01 ppm).
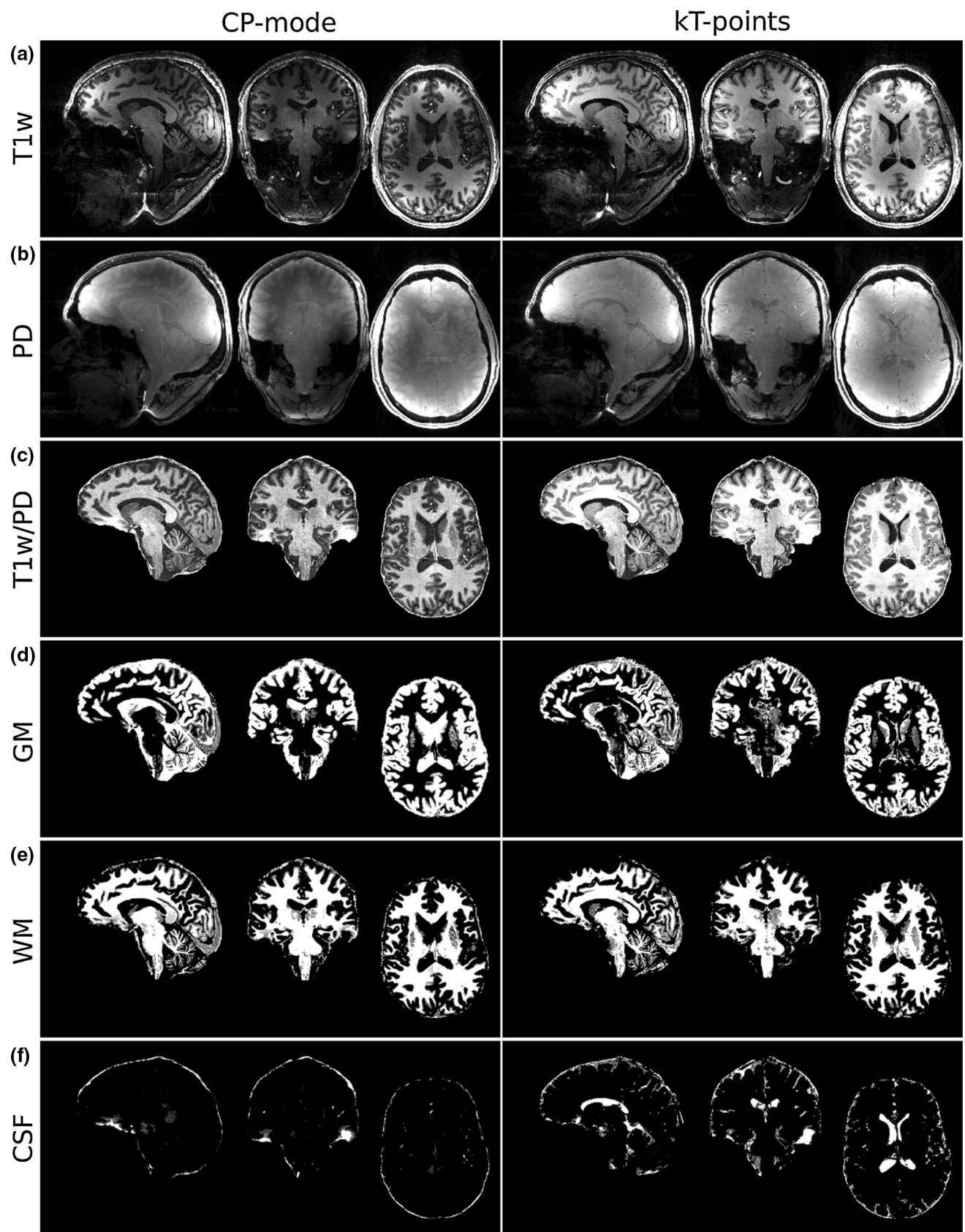
Fig. 7 a T_1-weighted MPRAGE image using TR-FOCI inversion and CP-mode excitation (*left column*) and kT-points excitation (*right column*). The intensities in both columns are scaled identically. **b** Proton density image using kT-points. **c** Brain extracted and receive bias corrected T_1-weighted image from **a** and **b**. **d**–**f** Grey matter, white matter and cerebrospinal fluid tissue probability maps extracted from **c** using FSL-FAST

Using the four additional 3rd order shim coils, the linewidth and the 90th percentile of the B_0 field distribution in the brain were on average further reduced by 14.7 and 16.9 %, respectively. This improvement is most apparent in the frontal regions of the brain as shown in Fig. 3d, e.

The second benefit of the homogenisation workflow is the reduction in signal and contrast variations across the image due to B_1^+ inhomogeneity which is a bigger challenge than B_0 homogenisation at 9.4 T. A previous simulation study on the same coil at 9.4 T has shown the limited capability of flip-angle homogenisation using static shim only [30]. By utilising the full 16-channel parallel RF transmission system dynamically, we were able to design kT-points pulse in the same brain region of interest to reduce the normalised RMSE of the excitation flip angle on average by 69.7 %, in comparison to CP-mode. All B_1^+ voids could be eliminated, as can be observed in Fig. 4. The Pre-Sat-TFL validation scans confirmed the agreement between the predicted and achieved flip angle distribution, and implicitly also the correct delivery of the pulse (e.g., gradient axis orientation, channel ordering, and phase sign).

The results over 6 scan sessions demonstrated that the improvements on both the B_0 and flip-angle homogenieties are consistent and reproducible. Various parts of the B_0 and flip-angle homogenisation procedure work in synergy with each other. Apart from reducing artefacts, a homogenised and known B_0 distribution can also ease the RF optimisation by narrowing the range of off-resonance in the problem. By excluding the subcutaneous tissue and the neck with the brain mask, the size of the RF optimisation problem is reduced and hence improves its speed and memory usage.

RF exposure to volunteers is a major concern in UHF MR, especially in combination with the use of parallel transmission. Using EM-simulations generated SAR matrices and VOPs compression, local SAR can be regularised during the pulse design process [59]. With the knowledge of the desired sequence parameters, the maximum local SAR can also be predicted in the pulse design workflow for a particular run of sequence [70]. The off-line maximum local SAR look-ahead allows the scanner operators to adjust the sequence parameters in order to keep the 10 s and 6 min exposure below the 20 W/kg and the 10 W/kg limits, respectively, as described in IEC 60601-2-33.

Several methods for B_0 and B_1 mapping have been shown in the literature for B_0 shim and RF pulse optimisations. It is out of the scope of this article to review or evaluate them, and the choices here were made based on pragmatic criteria: ease of implementation and effectiveness

Fig. 8 3D EPI images at 0.75 mm isotropic resolution, obtained using CP-mode (*top row*) and kT-points (*bottom row*) excitations

3D EPI
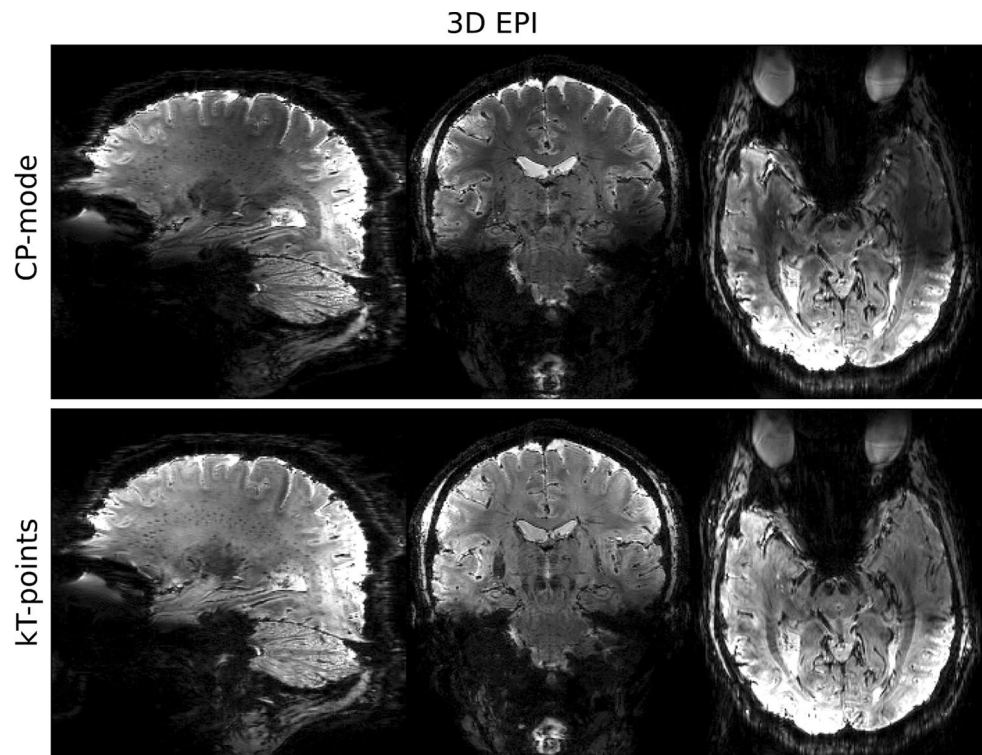
for the experimental setting (whole brain B_1 and B_0 shim). Shim current calculation for B_0 shims can, in principle, be achieved with a least-square fit expressed as a matrix inversion. However, the physical shim current limits need to be taken into account, for which we have chosen a constrained optimisation approach instead. For B_0 mapping, we have found that a standard dual-echo 3D GRE sequence, with phase unwrapping as shown in Ref [51], was fully sufficient for application in the brain, without apparent artefacts. For the RF optimisation, the main goal was in homogenising a low flip angle excitation pulse and we have hence chosen the STA approximation approach with a magnitude least square cost, due to its ease of obtaining a magnitude homogenised solution with a potential reduction in global RF power [35].

Two B_1 mapping sequences were use in this study, DREAM and PreSat-TFL. They were chosen for a couple of different aspects of B_1 mapping based on their different desired properties. The individual transmit channel B_1 maps were acquired with transmit phase encoded DREAM because of its speed, its insensitivity to B_0 variation and more robust against motion in comparison to PreSat-TFL. However, due to the RF pulse timing and layout in DREAM, it is not straightforward to map the kT-points pulses with it. Hence, a 2D PreSat-TFL, which is more flexible in terms of the mapping RF pulse, was used as the optional fast (20 s) qualitative validation of the designed pTx pulse. A full 3D quantitative mapping of the kT-points pulse is also possible by using an AFI [71] sequence, but this is not included in the current workflow because of its long acquisition time (~3 min).

The B_0 and B_1 maps collected during the session were also used in a Bloch simulation to decide which type of adiabatic pulse and what voltage amplitude was suitable for inversion in our imaging experiments. Our simulations have shown that the TR-FOCI inversion pulse performed better than the hyperbolic secant pulse provided in the standard product sequence, despite only using half the maximum transmitter voltage. Hence, TR-FOCI was chosen as the inversion pulse in our T_1-weighted MPRAGE for structural imaging and tissue segmentation. Despite its low adiabatic threshold, the TR-FOCI pulse in combination with a CP-like mode in this particular setup still could not provide a complete inversion throughout the region of interest defined by the brain mask. Using a large tip angle design as reported by [39, 72], the inversion efficiency can potentially be further improved. The feasibility of incorporating this approach into our B_0- and flip-angle-homogenisation is being investigated.

The efficient inversion of TR-FOCI in combination with the homogenised excitation through a kT-points pulse have led to significant improvement in the quality of the T_1-weighted MRRAGE images acquired at 9.4 T. As can be seen in the comparison of CP-mode and kT-points acquisitions of the T_1- and proton density weighted images shown in Fig. 7, the variations in intensity and contrast across the image were largely eliminated by substituting the standard rectangular pulses by parallel transmit kT-points excitations. Successful segmentation of the receive-bias-corrected images was achieved without further adjustment or manual intervention; this was not the case for the CP-mode acquired image.

Similar improvements were observed for the 3D EPI when comparing the CP-mode and kT-points acquired images. Similar improvements were observed for the 3D EPI when comparing the CP-mode and kT-points acquired images. While a 0.1 ms rectangular pulse is typically used in an MPRAGE readout train, a 1 ms pulse was used for the 3D EPI CP mode acquisition, because of the higher required flip angle and the lack of a time constraint. This "stretching" of the pulse proportionately reduced the required pulse amplitude, which explains the inversion of the local SAR estimates between the CP-mode and kT-points protocols for MPRAGE and 3D EPI listed in the Materials and Methods section. The increased pulse duration reduces the pulse bandwidth, which however remained much higher than the B_0 variations within the brain mask. Therefore most of the excitation inhomogeneity can be attributed to B_1 inhomogeneity from the transmit coils at this particular field strength.

Application of 3D EPI at 3 T and above has recently been receiving increased attention not only for BOLD imaging [45, 73, 74] but has also been shown to be an attractive choice for rapid acquisition of T_2^*-weighted structural data [75]. This can readily be extended to the application of SWI and QSM, as has recently been demonstrated at 3 T [76], 7 T and 9.4 T [77]. The benefits of 3D EPI are greatest at high-resolution which is particularly beneficial at UHF. A tremendous advantage of 3D sequences with two phase encoding directions is that they lend themselves to efficient parallel imaging undersampling strategies such as CAIPIRINHA [78] as has been shown also in the context of 3D EPI [79, 80].

The B_0 shim and RF pulse calculated by the B_0- and flip-angle-homogenisation workflow can be applied to other 3D scans such as GRE. The volumetric workflow has been extended to design slice-specific spokes pulses for 2D excitations as demonstrated in [81] for high in-plane resolution GRE imaging.

Conclusion

In summary, we demonstrated a B_0- and flip-angle-homogenisation procedure that currently takes approximately 15 min to run, and homogenises B_0 linewidth down to

0.10 ± 0.01 ppm and flip-angle normalised RMSE down to 9.2 ± 0.7 % in the same whole brain region of interest. This enables us to reduce intensity and contrast variations as well as distortions in our 9.4 T images.

Compliance with ethical standards

Conflict of interest   The authors declare that they have no conflict of interest.

Ethical approval   All procedures performed in studies involving human participants were in accordance with the ethical standards of the institutional and/or national research committee and with the 1964 Helsinki declaration and its later amendments or comparable ethical standards.

Informed consent   Informed consent was obtained from all individual participants included in the study.

References

1. Edelstein WA, Glover GH, Hardy CJ, Redington RW (1986) The intrinsic signal-to-noise ratio in NMR imaging. Magn Reson Med 3(4):604–618

2. Hoult DI, Richards RE (1976) The signal-to-noise ratio of the nuclear magnetic resonance experiment. J Magn Reson 24(1):71–85

3. Pohmann R, Speck O, Scheffler K (2015) Signal-to-noise ratio and MR tissue parameters in human brain imaging at 3, 7, and 9.4 tesla using current receive coil arrays. Magn Reson Med doi:10.1002/mrm.25677

4. Duyn JH (2012) The future of ultra-high field MRI and fMRI for study of the human brain. Neuroimage 62(2):1241–1248

5. Budde J, Shajan G, Scheffler K, Pohmann R (2014) Ultra-high resolution imaging of the human brain using acquisition-weighted imaging at 9.4T. Neuroimage 86:592–598

6. Duyn JH, van Gelderen P, Li TQ, de Zwart JA, Koretsky AP, Fukunaga M (2007) High-field MRI of brain cortical substructure based on signal phase. Proc Natl Acad Sci USA 104(28):11796–11801

7. Marques JP, van der Zwaag W, Granziera C, Krueger G, Gruetter R (2010) Cerebellar cortical layers: in vivo visualization with structural high-field-strength MR imaging. Radiology 254(3):942–948

8. Budde J, Shajan G, Zaitsev M, Scheffler K, Pohmann R (2014) Functional MRI in human subjects with gradient-echo and spin-echo EPI at 9.4 T. Magn Reson Med 71(1):209–218

9. van der Zwaag W, Francis S, Head K, Peters A, Gowland P, Morris P, Bowtell R (2009) fMRI at 1.5, 3 and 7 T: characterising BOLD signal changes. Neuroimage 47(4):1425–1434

10. Yacoub E, Shmuel A, Pfeuffer J, Van De Moortele PF, Adriany G, Andersen P, Vaughan JT, Merkle H, Ugurbil K, Hu X (2001) Imaging brain function in humans at 7 Tesla. Magn Reson Med 45(4):588–594

11. Bilgic B, Fan AP, Polimeni JR, Cauley SF, Bianciardi M, Adalsteinsson E, Wald LL, Setsompop K (2014) Fast quantitative susceptibility mapping with L1-regularization and automatic parameter selection. Magn Reson Med 72(5):1444–1459

12. Budde J, Shajan G, Hoffmann J, Ugurbil K, Pohmann R (2011) Human imaging at 9.4 T using T(2) *-, phase-, and susceptibility-weighted contrast. Magn Reson Med 65(2):544–550

13. Shmueli K, de Zwart JA, van Gelderen P, Li TQ, Dodd SJ, Duyn JH (2009) Magnetic susceptibility mapping of brain tissue in vivo using MRI phase data. Magn Reson Med 62(6):1510–1522

14. Wharton S, Bowtell R (2010) Whole-brain susceptibility mapping at high field: a comparison of multiple- and single-orientation methods. Neuroimage 53(2):515–525

15. Denk C, Hernandez Torres E, MacKay A, Rauscher A (2011) The influence of white matter fibre orientation on MR signal phase and decay. NMR Biomed 24(3):246–252

16. van Gelderen P, Mandelkow H, de Zwart JA, Duyn JH (2015) A torque balance measurement of anisotropy of the magnetic susceptibility in white matter. Magn Reson Med 74(5):1388–1396

17. Wiggins CJ, Gudmundsdottir V, Le Bihan D, V L MC (2015) Orientation dependence of white matter T2* contrast at 7T: a direct demonstration. In: Proceedings of the 23rd scientific meeting, International Society for Magnetic Resonance in Medicine, Toronto

18. Adriany G, Van de Moortele P-F, Ritter J, Moeller S, Auerbach EJ, Akgün C, Snyder CJ, Vaughan T, Ugurbil K (2008) A geometrically adjustable 16-channel transmit/receive transmission line array for improved RF efficiency and parallel imaging performance at 7 Tesla. Magn Reson Med 59(3):590–597

19. Barfuss H, Fischer H, Hentschel D, Ladebeck R, Oppelt A, Wittig R, Duerr W, Oppelt R (1990) In vivo magnetic resonance imaging and spectroscopy of humans with a 4 T whole-body magnet. NMR Biomed 3(1):31–45

20. Bomsdorf H, Helzel T, Kunz D, Röschmann P, Tschendel O, Wieland J (1988) Spectroscopy and imaging with a 4 tesla whole-body mr system. NMR Biomed 1(3):151–158

21. Bottomley PA, Andrew ER (1978) RF magnetic field penetration, phase shift and power dissipation in biological tissue: implications for NMR imaging. Phys Med Biol 23(4):630

22. Glover GH, Hayes CE, Pelc NJ, Edelstein WA, Mueller OM, Hart HR, Hardy CJ (1969) O?Donnell M, Barber WD (1985) Comparison of linear and circular polarization for magnetic resonance imaging. J Magn Reson 64(2):255–270

23. Keltner JR, Carlson JW, Roos MS, Wong STS, Wong TL, Budinger TF (1991) Electromagnetic fields of surface coil in vivo NMR at high frequencies. Magn Reson Med 22(2):467–480

24. Van de Moortele P-F, Akgun C, Adriany G, Moeller S, Ritter J, Collins CM, Smith MB, Vaughan JT, Ugurbil K (2005) B1 destructive interferences and spatial phase patterns at 7 T with a head transceiver array coil. Magn Reson Med 54(6):1503–1518

25. Vaughan T, DelaBarre L, Snyder C, Tian J, Akgun C, Shrivastava D, Liu W, Olson C, Adriany G, Strupp J, Andersen P, Gopinath A, van de Moortele P-F, Garwood M, Ugurbil K (2006) 9.4T human MRI: preliminary results. Magn Reson Med 56(6):1274–1282

26. O'Brien KR, Magill AW, Delacoste J, Marques JP, Kober T, Fautz HP, Lazeyras F, Krueger G (2014) Dielectric pads and low-B1+ adiabatic pulses: complementary techniques to optimize structural T1 w whole-brain MP2RAGE scans at 7 tesla. J Magn Reson Imaging 40(4):804–812

27. Teeuwisse WM, Brink WM, Webb AG (2012) Quantitative assessment of the effects of high-permittivity pads in 7 Tesla MRI of the brain. Magn Reson Med 67(5):1285–1293

28. Pauly J, Nishimura D (1969) Macovski A (1989) A k-space analysis of small-tip-angle excitation. J Magn Reson 81(1):43–56

29. Curtis AT, Gilbert KM, Klassen LM, Gati JS, Menon RS (2012) Slice-by-slice B1 + shimming at 7 T. Magn Reson Med 68(4):1109–1116

30. Hoffmann J, Shajan G, Scheffler K, Pohmann R (2014) Numerical and experimental evaluation of RF shimming in the human brain at 9.4 T using a dual-row transmit array. Magn Reson Mater Phy 27 (5):373–386

31. Mao W, Smith MB, Collins CM (2006) Exploring the limits of RF shimming for high-field MRI of the human head. Magn Reson Med 56(4):918–922

32. Grissom W, Yip C-Y, Zhang Z, Stenger VA, Fessler JA, Noll DC (2006) Spatial domain method for the design of RF pulses in multicoil parallel excitation. Magn Reson Med 56(3):620–629

33. Katscher U, Börnert P, Leussler C, van den Brink JS (2003) Transmit SENSE. Magn Reson Med 49(1):144–150

34. Zhu Y (2004) Parallel excitation with an array of transmit coils. Magn Reson Med 51(4):775–784

35. Setsompop K, Wald LL, Alagappan V, Gagoski BA, Adalsteinsson E (2008) Magnitude least squares optimization for parallel radio frequency excitation design demonstrated at 7 Tesla with eight channels. Magn Reson Med 59(4):908–915

36. Cloos MA, Boulant N, Luong M, Ferrand G, Giacomini E, Le Bihan D, Amadon A (2012) kT -points: short three-dimensional tailored RF pulses for flip-angle homogenization over an extended volume. Magn Reson Med 67(1):72–80

37. Malik SJ, Keihaninejad S, Hammers A, Hajnal JV (2012) Tailored excitation in 3D with spiral nonselective (SPINS) RF pulses. Magn Reson Med 67(5):1303–1315

38. Mugler JP 3rd, Brookeman JR (1991) Rapid three-dimensional T1-weighted MR imaging with the MP-RAGE sequence. J Magn Reson Imaging 1(5):561–567

39. Cloos MA, Boulant N, Luong M, Ferrand G, Giacomini E, Hang MF, Wiggins CJ, Le Bihan D, Amadon A (2012) Parallel-transmission-enabled magnetization-prepared rapid gradient-echo T1-weighted imaging of the human brain at 7 T. Neuroimage 62(3):2140–2150

40. Hans Hoogduin RMGMJVHPL (2014) Malik SJ Initial experience with SPIral Non Selective (SPINS) RF pulses for homogeneous excitation at 7T. Proceedings of the 22nd scientific meeting. International Society for Magnetic Resonance in Medicine, Milan, p 4914

41. Jezzard P, Balaban RS (1995) Correction for geometric distortion in echo planar images from B0 field variations. Magn Reson Med 34(1):65–73

42. Frahm J, Merboldt KD, Hanicke W (1994) The influence of the slice-selection gradient on functional MRI of human brain activation. J Magn Reson B 103(1):91–93

43. Speck O, Stadler J, Zaitsev M (2008) High resolution single-shot EPI at 7T. Magn Reson Mater Phy 21(1–2):73–86

44. Pan JW, Lo K-M, Hetherington HP (2012) Role of very high order and degree B0 shimming for spectroscopic imaging of the human brain at 7 tesla. Magn Reson Med 68(4):1007–1017

45. Poser BA, Koopmans PJ, Witzel T, Wald LL, Barth M (2010) Three dimensional echo-planar imaging at 7 Tesla. Neuroimage 51(1):261–266

46. Shajan G, Kozlov M, Hoffmann J, Turner R, Scheffler K, Pohmann R (2014) A 16-channel dual-row transmit array in combination with a 31-element receive array for human brain imaging at 9.4 T. Magn Reson Med 71(2):870–879

47. Gumbrecht R, Fontius U, Adolf H, Benner T, Schmitt F, Adalsteinsson E, Wald LL, H.-P. F (2013) Online Local SAR Supervision for Transmit Arrays at 7T In: Proceedings of the 21st scientific meeting, International Society for Magnetic Resonance in Medicine, Salt Lake City

48. Hoffmann J, Henning A, Giapitzakis IA, Scheffler K, Shajan G, Pohmann R, Avdievich NI (2015) Safety testing and operational procedures for self-developed radiofrequency coils. NMR Biomed. doi:10.1002/nbm.3290

49. Eichfelder G, Gebhardt M (2011) Local specific absorption rate control for parallel transmission by virtual observation points. Magn Reson Med 66(5):1468–1476

50. Poole MS, Panchuelo RS, Panel R, Peters A, Bowtell R (2011) Benefits of Brain Segmentation and 3D Field Mapping in B0 Shimming at 7T. ISMRM Scientific Workshop: Ultra-High Field Systems and Applications: 7T and Beyond: Progress. Lake Louise, Pitfalls and Potential, p 34

51. Cusack R, Papadakis N (2002) New robust 3-D phase unwrapping algorithms: application to magnetic field mapping and undistorting echoplanar images. Neuroimage 16(3 Pt 1):754–764

52. Grant M, Boyd S (2008) Graph implementations for nonsmooth convex programs. In: Blondel V, Boyd S, Kimura H (eds) Recent Advances in Learning and Control. Springer-Verlag Limited

53. Grant M, Boyd S (2014) CVX: Matlab Software for Disciplined Convex Programming, version 2.1

54. Smith SM (2002) Fast robust automated brain extraction. Hum Brain Mapp 17(3):143–155

55. Tse DHY, Poole MS, Magill AW, Felder J, Brenner D, Jon Shah N (2014) Encoding methods for B1(+) mapping in parallel transmit systems at ultra high field. J Magn Reson 245:125–132

56. Nehrke K, Versluis MJ, Webb A, Bornert P (2014) Volumetric B1 (+) mapping of the brain at 7T using DREAM. Magn Reson Med 71(1):246–256

57. Chung S, Kim D, Breton E, Axel L (2010) Rapid B1 + mapping using a preconditioning RF pulse with TurboFLASH readout. Magn Reson Med 64(2):439–446

58. Sbrizzi A, Hoogduin H, Lagendijk JJ, Luijten P, SGL G, van den Berg CAT (2011) Time efficient design of multi dimensional RF pulses: application of a multi shift CGLS algorithm. Magn Reson Med 66(3):879–885

59. Sbrizzi A, Hoogduin H, Lagendijk JJ, Luijten P, Sleijpen GLG, van den Berg CAT (2012) Fast design of local N-gram-specific absorption rate?optimized radiofrequency pulses for parallel transmit systems. Magn Reson Med 67(3):824–834

60. Poole MS, Tse DHY, Vahedipour K, Shah NJ (2014) A region growing algorithm for robust kt-points B1 + homogenisation at 9.4T. In: Proceedings of the 22nd scientific meeting, International Society for Magnetic Resonance in Medicine, Milan

61. Amadon A, Dupas L, Vignaud A (2015) Boulant N Does the best distance beween 2 spokes match the inverse RF wavelength? Proceedings of the 23rd scientific meeting. International Society for Magnetic Resonance in Medicine, Toronto, p 2388

62. Hurley AC, Al-Radaideh A, Bai L, Aickelin U, Coxon R, Glover P, Gowland PA (2010) Tailored RF pulse for magnetization inversion at ultrahigh field. Magn Reson Med 63(1):51–58

63. Zhang Y, Brady M, Smith S (2001) Segmentation of brain MR images through a hidden Markov random field model and the expectation-maximization algorithm. IEEE Trans Med Imaging 20(1):45–57

64. Van de Moortele PF, Auerbach EJ, Olman C, Yacoub E, Ugurbil K, Moeller S (2009) T1 weighted brain images at 7 Tesla unbiased for Proton Density, T2* contrast and RF coil receive B1 sensitivity with simultaneous vessel visualization. Neuroimage 46(2):432–446

65. Ivanov D, Barth M, Uludag K (2015) Poser BA Robust ACS acquisition for 3D echo planar imaging. Proceedings of the 23rd scientific meeting. International Society for Magnetic Resonance in Medicine, Toronto, p 2059

66. Jesmanowicz A, Wong E, J. H (1993) Phase correction for EPI using internal reference lines. In: Proceedings of the 12th scientific meeting, International Society for Magnetic Resonance in Medicine, Kyoto

67. Pfeuffer J, Van de Moortele PF, Ugurbil K, Hu X, Glover GH (2002) Correction of physiologically induced global off-resonance effects in dynamic echo-planar and spiral functional imaging. Magn Reson Med 47(2):344–353

68. Silver MS, Joseph RI, Hoult DI (1985) Selective spin inversion in nuclear magnetic resonance and coherent optics through an exact solution of the Bloch-Riccati equation. Phys Rev A 31(4):2753–2755

69. Jezzard P (2012) Correction of geometric distortion in fMRI data. Neuroimage 62(2):648–651

70. Graesslin I, Homann H, Biederer S, Bornert P, Nehrke K, Vernickel P, Mens G, Harvey P, Katscher U (2012) A specific absorption rate prediction concept for parallel transmission MR. Magn Reson Med 68(5):1664–1674

71. Nehrke K (2009) On the steady-state properties of actual flip angle imaging (AFI). Magn Reson Med 61(1):84–92

72. Cao Z, Donahue MJ, Ma J, Grissom WA (2015) Joint design of large-tip-angle parallel RF pulses and blipped gradient trajectories. Magn Reson Med. doi:10.1002/mrm.25739

73. Lutti A, Thomas DL, Hutton C, Weiskopf N (2013) High-resolution functional MRI at 3 T: 3D/2D echo-planar imaging with optimized physiological noise correction. Magn Reson Med 69(6):1657–1664

74. van der Zwaag W, Marques JP, Kober T, Glover G, Gruetter R, Krueger G (2012) Temporal SNR characteristics in segmented 3D-EPI at 7T. Magn Reson Med 67(2):344–352

75. Zwanenburg JJ, Versluis MJ, Luijten PR, Petridou N (2011) Fast high resolution whole brain T2* weighted imaging using echo planar imaging at 7T. Neuroimage 56(4):1902–1907

76. Langkammer C, Bredies K, Poser BA, Barth M, Reishofer G, Fan AP, Bilgic B, Fazekas F, Mainero C, Ropele S (2015) Fast quantitative susceptibility mapping using 3D EPI and total generalized variation. Neuroimage 111:622–630

77. Poser BA, Ivanov D, Barth M, Uludag K (2015) High-resolution 3D EPI at 7 and 9.4T and its application to quantitative susceptibility mapping. In: Proceedings of 19th Annual Meeting, Organization for Human Brain Mapping, Honolulu

78. Breuer FA, Blaimer M, Mueller MF, Seiberlich N, Heidemann RM, Griswold MA, Jakob PM (2006) Controlled aliasing in volumetric parallel imaging (2D CAIPIRINHA). Magn Reson Med 55(3):549–556

79. Poser BA, Kemper VG, Ivanov D, Kannengiesser SA, Uludag K (2013) Barth M CAIPIRINHA-accelerated 3D EPI for high temporal and/or spatial resolution EPI acquisitions. Proceedings of 30th Annual Scientific Meeting. European Society for Magnetic Resonance in Medicine and Biology, Toulouse, p 287

80. Zahneisen B, Ernst T, Poser BA (2015) SENSE and simultaneous multislice imaging. Magn Reson Med 74(5):1356–1362

81. Tse DHY, Brenner D, Guerin B, Poser BA (2015) High resolution GRE at 9.4T using spokes pulses. In: Proceedings of the 23rd scientific meeting, International Society for Magnetic Resonance in Medicine, Toronto